PREDICTION OF THE THRUST PERFORMANCE AND THE FLOWFIELD OF LIQUID ROCKET ENGINES

T.-S. Wang
Computational Fluid Dynamics Branch
NASA Marshall Space Flight Center
Marshall Space Flight Center, AL

ABSTRACT

In an effort to improve the current solutions in the design and analysis of liquid propulsive engines, a computational fluid dynamics (CFD) model capable of calculating the reacting flows from the combustion chamber, through the nozzle to the external plume, was developed. The Space Shuttle Main Engine (SSME) fired at sea level, was investigated as a sample case. The CFD model, FDNS, is a pressure based, non-staggered grid, viscous/inviscid, ideal gas/real gas, reactive code. An adaptive upwinding differencing scheme is employed for the spatial discretization. The upwind scheme is based on fourth order central differencing with fourth order damping for smooth regions, and second order central differencing with second order damping for shock capturing. It is equipped with a CHMQGM equilibrium chemistry algorithm and a PARASOL finite rate chemistry algorithm using the point implicit method. In this study, the computed flow results and performance compared well with those of other standard codes and engine hot fire test data. In addition, the transient nozzle flowfield calculation was also performed to demonstrate the ability of FDNS in capturing the flow separation during the startup process.

INTRODUCTION

Several limitations have been found with the current industrial standards in calculating the flowfield and performance of liquid rocket engines. For example, the Method of Characteristics (MOC) was generally used to analyze the supersonic nozzle flowfield; however, factors that could influence the numerical results included transonic flow analysis, the location and flow properties of the start line, along with the number and distribution of points on the start line. Moreover, MOC is restricted to supersonic flow. Composite codes and decoupled solutions have to be resorted to resolve the wall boundary layer, the combustion chamber flow, and the exhaust plume. Limitations in axisymmetric formulations and steady-state solutions are two other shortcomings. The recent advancement of CFD technology has shown potentials in transient flow simulations (ref. 1), flow reversal prediction capabilities, and a unified solution (ref. 2) for subsonic, transonic and supersonic flowfields. Furthermore, general two dimensional and three dimensional geometry can be described; and applications to dual throat engines, scarfed and integrated nozzles, and cluster nozzles may be achieved. This study produced a CFD model for the description of the unified liquid rocket engine flowfields, and the prediction of the thrust performance with the unified solution. Code validation was achieved by choosing SSME firing at 100% power at sea level as the sample case, and by verifying the code from such options as ideal gas, inviscid, non-reacting, adiabatic wall to a more complicated real gas, viscous, equilibrium, and specified wall temperature calculation. The computed results were compared to those of various industrial CFD codes and hot fire experiments. Finally, a transient calculation was performed to demonstrate the CFD code's ability in capturing the shock evolution and the flow separation during the transient operation.

GOVERNING EQUATIONS

The basic equations employed to describe a unified liquid rocket engine flowfield are the axisymmetric, multi-component transport equations. The classification of the governing equations changes from one point to another in the unified flowfield. That is, elliptic for subsonic flow, parabolic for sonic flow, and hyperbolic for supersonic flow. A generalized form of these equations written in curvilinear coordinates is given by

$$(1/J)(\partial \rho q/\partial t) = \partial[-\rho U_i q + \nu G_{ij}(\partial q/\partial \xi_j)]/\partial \xi_i + S_q \qquad (1)$$

where J, U_i and G_{ij} are the Jacobian of coordinate transformation, the contravariant velocity and the geometrical matrices. q represents 1, u, v, h, k, ϵ and ρ_i,

---

respectively. These are equations of continuity, x and y momentum, enthalpy, turbulent kinetic energy, turbulent kinetic energy dissipation rate, and density fractions. The effective eddy viscosity ν is determined by solving a extended two-equation k-ε turbulence model (refs. 3 and 4). Source terms S_q are given by

$$S_q = 1/J \begin{bmatrix} 0 \\ -p_x + \nabla[\nu(u_j)_x] - 2/3(\nu\nabla u_j)_x \\ -p_y + \nabla[\nu(u_j)_y] - 2/3(\nu\nabla u_j)_y \\ Dp/Dt + \Phi + \Sigma J_n C_{pn}\nabla T - \Sigma h_n W_n \\ \rho(P_r - \varepsilon) \\ \rho(\varepsilon/k)(C_1 P_r - C_2\varepsilon + C_3 P_r^2/\varepsilon) \\ W_n, \quad n = 1,\ldots,N \end{bmatrix} \tag{2}$$

where Φ is the energy dissipation function, J_n is diffusion flux, C_{pn} is heat capacity, and W_n denotes mass production rate for species n. P_r represents the turbulent kinetic energy production term. C_1, C_2 and C_3 are model constants for the two-equation turbulence model.

NUMERICAL SCHEMES

An adaptive upwinding scheme was employed to approximate the convective terms of the momentum, energy and continuity equations; the scheme is based on second and fourth order central differencing with artificial dissipation. First order upwinding is used for species and turbulence equations, since the parameters involved are positive quantities. Different eigenvalues are used for weighing the dissipation terms depending on the conserved quantity being evaluated, in order to give correct diffusion fluxes near wall boundaries. Adding the dissipation term to the convective fluxes F in computational coordinate ξ produces

$$\partial F/\partial \xi \simeq (F_{i+1} - F_{i-1})/2 - (d_{i+1/2} - d_{i-1/2}) \tag{3}$$

The dissipation term, d, is constructed such that a fourth-order central and fourth-order damping scheme is activated in smooth regions, and a second-order central and second-order damping scheme is used near shock waves. Since the Jacobian matrices of the Euler fluxes have eigenvalues of U, U+c and U-c, it is sufficient to use the magnitudes of these eigenvalues to weigh the dissipation terms to maintain the smoothness of the solution without losing accuracy. $|U|+c$ was used for the continuity equation and $|U|$ was used for other transport equations in FDNS. A general form of the dissipation term is given by

$$d_{i+1/2} = 0.25[2\varepsilon_1|\rho U| + \varepsilon_2(|U| + c)]_{i+1/2}(q_{i+1} - q_i)$$

$$+ [\varepsilon_3(1 - \varepsilon_1)MAX[0.5f\rho(|u| + |v|),2|\rho U|]$$

$$+ \varepsilon_4(|U| + c)]_{i+1/2}(q_{i-1} - 3q_i + 3q_{i+1} - q_{i+2}) \tag{4}$$

where $a_i = |p_{i+1} - 2p_i + p_{i-1}|/(p_{i+1} + 2p_i + p_{i-1})$

$\theta_{i+1/2} = MAX(a_i, a_{i+1})$

$d_1 = MAX[\lambda, MIN(1.0, 25\theta_{i+1/2})]$

$d_4 = MAX(0.0, 0.01 - 0.25\theta_{i+1/2})$

Different values for dissipation parameters ε_1, ε_2, ε_3 and ε_4 are used for the continuity, energy and momentum transport equations. f represents a local cell flow area. Unity λ corresponds to a fully upwinded differencing scheme and vanishing λ corresponds to a central differencing scheme for the convective terms in smooth regions. Table I summarizes these parameters.

Table I. Dissipation Parameters

	Momentum & Energy	Continuity
ε_1	d_1	0
ε_2	0	$\theta_{i+1/2}$
ε_3	0.015	0
ε_4	0	d_4

A pressure based method was selected such that a wide range of flow speeds could be analyzed with the same code. Successful results of viscous flow computations using pressure based methods have been reported (refs. 5 and 6). For high speed flow cases, a hyperbolic pressure correction equation was employed by perturbing the density in the mass conservation equation. This provides a smooth transition from low to high speed flow characteristics. For time accuracy, a time-centered, time-marching scheme with a multiple pressure corrector algorithm was employed. In general, a noniterative time-marching scheme was used for time dependent flow computations (ref. 1); however, subiterations can be used if necessary. The multi-corrector procedure will be described below.

A simplified momentum equation was combined with the continuity equation to form a pressure correction equation. The simplified momentum equation can be written as:

$$\partial \rho u_i/\partial t \simeq - \nabla p'$$

or, in discrete form,

$$u'_i \simeq - \beta(\Delta t/\rho)\nabla p' \tag{5}$$

where β represent a pressure relaxation parameter. The velocity and density fields in the continuity equation are then perturbed to form a correction equation. That is,

$$[\partial \rho/\nabla t + \nabla(\rho u_i)]^{n+1} = \partial(\rho^n + \rho')/\partial t + \nabla[(\rho^n + \rho')(u^n_i + u'_i)] = 0$$

By neglecting the $\rho'u'$ terms, the following equation results.

$$\partial \rho'/\partial t + \nabla(u_i\rho') + \nabla(\rho u'_i) = - [\partial \rho/\partial t + \nabla(\rho u_i)]^n \tag{6}$$

Substituting Eq. (5) into Eq. (6) and letting $\rho' = p'/RT$, the following pressure correction equation is obtained.

$$\partial(p'/RT)/\partial t + \nabla[(u_i/RT)p'] - \nabla(\beta\Delta t \nabla p') = - [\partial \rho/\partial t + \nabla(\rho u_i)]^n \tag{7}$$

To provide smooth shock solutions the adaptive dissipation terms described above were added to the right hand side of Eq. (7). Once Eq. (7) is satisfied, the velocity field and the pressure field are updated through Eq. (5) and the following relation.

$$p^{n+1} = p^n + p'$$

The density field is then updated by applying the equation of state. To ensure that the updated velocity, density and pressure fields satisfy the continuity equation, the above pressure correction solution procedure is repeated several times before marching to the next time step. This represents a multi-corrector solution procedure.

The chemistry source terms were evaluated with a point implicit procedure before the species equations were solved. The determination of equilibrium chemistry source terms were based on the CHMQGM algorithm (ref. 7).

CHMQGM EQUILIBRIUM CHEMISTRY ALGORITHM

The chemistry source terms must be computed for each grid point at each time step. The point implicit procedure allows the equilibrium calculation for each grid point to be independent from that of its neighbors and may be treated in isolation. Since kinetics loss was estimated to be negligible in the SSME thrust chamber and

135

nozzle (ref. 8), equilibrium is assumed to exist for the entire computational domain, including the exhaust plume region.

In general, if there are N distinct chemical species composed of M chemical elements, then the algebraic system to be solved consists of N-M nonlinear equilibrium equations and M linear element-conservation relations. Let A_i be the chemical symbol of the ith species. While a_{is} and b_{is} stand for the stoichiometric coefficients for the forward and backward reactions. The equilibrium reactions are of the form

$$\sum_{i=1}^{N} a_{is} A_i = \sum_{i=1}^{N} b_{is} A_i, \qquad s=1,\ldots N-M$$

The equilibrium reactions lead to algebraic relations of the form

$$K_s \prod_{i=1}^{N} [c_i]^{a_{is}} = \prod_{i=1}^{N} [c_i]^{b_{is}}, \qquad s=1,\ldots N-M \qquad (8)$$

where K_s is equilibrium constant for sth reaction. The linear element-conservation reactions are of the form

$$\sum_{i=1}^{N} d_{ij} c_i = C_j \qquad j=1,\ldots M \qquad (9)$$

where c_i is species molar concentration, C_j denotes element molar concentration and d_{ij} represents the number of element in a species.

CHMQGM algorithm has shown that a reduced system can be obtained by substituting the M linear relations, Eq.(9), into the N-M nonlinear relations, Eq.(8). As a result, a iterative Newton-Raphson technique was used to solve a system of N-2M equations rather than the larger equivalent NxN system. The equilibrium constant approach of CHMQGM is not as general as a minimization of Gibb's free energy approach (ref. 9) for an arbitrary chosen chemical system. However, for a generally well-known hydrogen/oxygen system such as the one being used in SSME, CHMQGM appears to be more efficient.

HYDROGEN/OXYGEN EQUILIBRIUM CHEMISTRY

The Hydrogen/Oxygen equilibrium reactions used in this study is a subset reduced from the hydrocarbon combustion partial equilibrium system (ref. 7). It consists of six species and four reactions as shown in Table II.

Table II. Species and reactions considered

Subscript		Species	Subscript		Species
1	H2O	Water vapor	4	OH	Hydroxyl radical
2	H	Atomic hydrogen	5	H_2	Molecular hydrogen
3	O	Atomic oxygen	6	O_2	Molecular oxygen

$$O_2 = 2O \qquad\qquad K_1 c_6 = (c_3)^2 \qquad\qquad (10)$$

$$H_2 = 2H \qquad\qquad K_2 c_5 = (c_2)^2 \qquad\qquad (11)$$

$$2OH = O_2 + H_2 \qquad K_3 (c_4)^2 = c_6 c_5 \qquad\qquad (12)$$

$$2H_2O = 2H_2 + O_2 \qquad K_4 (c_1)^2 = (c_5)^2 c_6 \qquad (13)$$

The element-conservation equations are

$$C_O = c_1 + c_3 + c_4 + 2c_6 \qquad\qquad (14)$$

$$C_H = 2c_1 + c_2 + c_4 + 2c_5 \qquad\qquad (15)$$

Substitute Eq.(10) and Eq.(11) to Eq.(12) and Eq.(13), we have

$$c_6 = R_1 (c_3)^2 \qquad R_1 = 1/K_1 \qquad\qquad (16)$$

136

$$c_5 = R_2(c_2)^2 \qquad R_2 = 1/K_2 \qquad\qquad (17)$$

$$c_4 = R_3 c_2 c_3 \qquad R_3 = 1/(K_1 K_2 K_3)^{1/2} \qquad\qquad (18)$$

$$c_1 = R_4 c_5 c_3 \qquad R_4 = 1/(K_1 K_4)^{1/2} \qquad\qquad (19)$$

Substitute the linear term in equations (16-19) into the linear element-conservation equations (14 and 15), yielding two nonlinear equations and three unknowns in c_2, c_3, and c_5.

$$C_0 = R_4 c_5 c_3 + c_3 + R_3 c_2 c_3 + 2R_1(c_3)^2 \qquad\qquad (20)$$

$$C_H = 2R_4 c_5 c_3 + c_2 + R_3 c_2 c_3 + 2R_2(c_2)^2 \qquad\qquad (21)$$

The final reduced equations can then be obtained by substituting Eq.(20) to Eq.(21) and to eliminate c_5 in Eq.(20) with Eq.(17), we have

$$R_2 R_4 (c_2)^2 c_3 + R_3 c_2 c_3 + 2R_1(c_3)^2 + c_3 - C_0 = 0$$

and

$$R_3 c_2 c_3 + 4R_1(c_3)^2 + 2c_3 - 2R_2(c_2)^2 - c_2 + (C_H - 2C_0) = 0$$

This reduced system consists of one cubic equation and one quadratic equation with two unknowns, and can readily be solved by Newton-Raphson's iterative method.

BOUNDARY CONDITIONS

Fixed chamber conditions were used at the inlet of the combustion chamber. Subsonic boundary conditions were used at the inlet of the external ambient air and the pressure was extrapolated. This is to allow the transient disturbances sent from downstream to permeate through the boundary. Flow properties at the wall, centerline and exit were extrapolated from those of the interior domain. To obtain a unique solution for the SSME sample case at sea level, a fixed pressure was applied to the outermost point of the downstream ambient exit boundary. A wall temperature distribution (ref. 2) was specified for the viscous, real gas, and regeneratively cooled wall calculation. For transient thrust chamber and plume flowfield calculations, a digital transient model simulation (DTM) was used as the combustor upstream boundary conditions.

SAMPLE CASES FOR SSME AT 100% POWER LEVEL

SSME operating conditions at 100% power level and sea level were used for the calculations. The actual values used are shown in Table III.

Table III. Operating Parameters

Mixture Ratio	6.000
O2 inlet temperature (K)	90.56
H2 inlet temperature (K)	20.56
Chamber Pressure (PSIA)	2935.7
Chamber Temperature (K)	3639.0
Geometric Area Ratio	77.5

RESULTS

INVISCID, IDEAL GAS, AND ADIABATIC WALL CALCULATION

FDNS calculations were made for the inviscid, ideal gas and adiabatic wall conditions in order to compare to the equivalent MOC solutions. The domain of computation was started from the injector faceplate, through the throat and ended at the nozzle exit plane. Computational results obtained from running the PARC code (ref. 10) was also used for comparison. Cases for different specific heat capacity ratios (γ=1.14, 1.1875 and 1.25) were performed. Fig. 1 shows the comparison of vector and Mach number contour for FDNS and PARC solutions at γ=1.1875. The vectors showed a transition from subsonic flow in the main combustor to sonic flow at the throat, and to supersonic flow in the nozzle. While FDNS used a pressure based method, PARC used a density based procedure. Both codes have captured the nozzle shock stemming downstream from the throat, and exhibited similar Mach number contours throughout the computational domain. A sonic line can be observed near the throat

region. The computations were made on the same grid with a grid size of 111x65.

Fig. 2 shows the comparison of centerline and wall pressure distributions for $\gamma=1.1875$. The FDNS predictions compared well with those of the MOC and PARC results. The sonic start lines obtained from FDNS calculations were used for MOC calculations. The computational time for a typical FDNS ideal gas calculation was estimated as 1.03E-4 CPU seconds per grid per step on a NASA/MSFC CRAY-XMP. Five hundred iterations were required for approximate convergence.

Performance calculations showed specific impulses (ISP) of 426.6, 452.5, and 472.3 for $\gamma=1.25$, 1.1875 and 1.14, respectively. Real gas calculations indicated that the heat capacity ratio ranged from 1.14 at the combustor inlet, to about 1.25 at the nozzle exit. The thermodynamic properties of the combusting gases are very important parameters to the accurate prediction of the liquid rocket engine flowfields and performance. A real gas thermodynamics calculation is therefore in order.

INVISCID, REAL GAS, AND ADIABATIC WALL CALCULATION

The computational domain was extended to include the exhaust plume, and the ambient air for the low altitude FDNS real gas calculations. Seven species were considered. Including H_2, O_2, H_2O, O, H, OH and N_2. Chemical equilibrium was assumed to be valid for the entire flowfield. Fig. 3 shows the comparison of FDNS and MOC predicted centerline and wall Mach numbers. MOC used equilibrium properties table obtained from CEC thermal equilibrium calculations (ref. 9). The FDNS predicted centerline Mach numbers agreed well with those of the MOC prediction. The FDNS predicted wall Mach number matched MOC calculation from approximately the center of the nozzle to the exit plane, but underpredicted near the throat. The underprediction may have been caused by two reasons: First, a constant perpendicular sonic start line (Mach number=1.01) was assumed for the MOC calculation that was different from the FDNS calculated sonic line; second, the artificial dissipation used to capture shock by FDNS may have generated some total pressure loss, near the starting point of the nozzle shock at the wall, and as a result, the underprediction of the Mach number near the throat. Nevertheless, the Mach number comparison for the FDNS and MOC was reasonably good. Fig. 4 shows the comparison of centerline and wall pressure distributions. The FDNS predicted centerline and wall pressures agreed well with those of the MOC predictions. RAMP code (ref. 11), overpredicted the centerline pressure slightly near the exit plane.

The FDNS predicted SSME nozzle specific impulse is compared to that of MOC and TDK predictions in Table IV. TDK calculation (ref. 8) used an eight-reaction finite rate kinetics mechanism. The closeness of all three ISP values indicated that the kinetics loss and shock-kinetics interaction is probably negligible under these circumstances. The computational time for a typical FDNS real gas calculation was estimated to be 2.36E-4 CPU seconds per grid per step. Approximately Twenty-five hundred iterations were required for near convergence. The grid size used in this calculation was 201x81.

Table IV. ISP comparison

Code	ISP	Chemistry
FDNS	460.4	CHMQGM
MOC	458.4	CEC
TDK	459.2	Finite Rate

VISCOUS, REAL GAS, AND COOLED WALL CALCULATION

The simulation of 100% power level SSME fired at sea level, was completed by adding the viscous terms and a specified wall temperature to the FDNS calculation. The extended k-ε turbulence model and wall function approach were used to calculate the viscous flow. The specified wall temperature was obtained from ref. 8. Fig. 5 shows the Mach number contour of a FDNS calculated conical nozzle flow. The operating conditions were identical to that of the bell-shaped SSME nozzle as indicated in Table III, including the nozzle length and the area ratio. This was to see if the pressure based FDNS CFD model can capture a perfect normal shock from a nearly one dimensional nozzle flow. From Fig. 5, a nozzle shock formed after the inflection point, hit the centerline, and reflected inside the nozzle; a lip shock formed at the nozzle exit and extended to the triple point in the plume region, where a Mach disc dropped beneath the triple point and perpendicular to the axis.

The computed Mach number contour of the overexpanded SSME nozzle flowfield is shown in Fig. 6. Unlike the one-dimensional conical nozzle flow, a distinctive two-dimensional flow behavior is observed. A slightly curved Mach disc developed in the plume region; the chamber total temperature was recovered behind the Mach disc. The disc location was estimated to be 1.1 nozzle exit radii from the exit plane, with a width of about 1.1 nozzle exit radii. The location and width of the computed normal disc agreed well with those of the hot fire test (ref. 12). The thrust performance comparison of the experimental data, the FDNS and TDK/BLM results are shown in Table V. BLM is a boundary layer code that provides TDK with the boundary layer solution. The FDNS calculated ISP value compared very well with that of the hot fire test (ref. 13) and the TDK/BLM calculation.

Table V. ISP comparison

	ISP	Chemistry
Experiment	453.3	
FDNS	453.4	CHMQGM
TDK/BLM	452.3	Finite Rate

The typical grid size used in this calculation was identical to that of the inviscid case. The computational time for one typical run was 2.77E-4 CPU seconds per grid per step. Approximately Three thousand iterations were required for near convergence. The CPU time for a nonreacting case was 2.32E-4 seconds per grid per step. That means only about 20% increase for a equilibrium chemistry calculation.

TRANSIENT SSME THRUST CHAMBER AND PLUME FLOWFIELD CALCULATION

The existing SSME thrust chamber was designed to give optimum performance under the constraint that the nozzle lip pressure is fixed around 5.5 PSI. This pressure was selected to avoid flow separation at sea level during full power level. The vector plot of CFD calculations showed no flow separation under these operation conditions, as presented in Fig. 1. Asymmetric flow separation during transient operation is then the phenomena of prime interest, since the resultant side forces could be highly detrimental to the engine. As a first attempt, a transient calculation was performed on a axisymmetric grid to study the flow separation inside a nozzle.

The transient thrust chamber and plume flowfield was calculated as a viscous, real gas, and reacting (CHMQGM) flow calculation. The regeneratively cooled wall temperature distribution was assumed to be the same as that of the steady state case. The grid domain used was also identical. To simulate the actual hot fire operation, DTM simulation was used to generate the transient upstream boundary conditions. These transient upstream flow properties included temperature, pressure, and propellants flow rates at the injector end. The igniter flow and the coolant flow were combined with the main injector flow to account for the total flow rate. Sea level pressure and temperature were used as ambient properties.

Pressure contours at different time cuts are shown in Fig. 7a-7f. Fig. 7a shows the pressure contour at 1.58 seconds. It can be seen that a normal shock wave was moving down the thrust chamber. This strong shock imposed a large adverse pressure gradient in the nozzle. As the boundary layer was not able to negotiate this adverse pressure gradient due to wall friction, the flow separated at the foot of the rear oblique shock. Another front oblique shock stemmed from the triple point, albeit it is somewhat smeared by the encroachment of the back flow. A nozzle shock can be seen developing from the inflection point near the throat. Fig. 7b shows the progress at 2.13 seconds. The strong shock moved down some more and the flow separation persisted. Fig. 7c occurred at 2.53 seconds. The developing nozzle shock that hit the centerline may have strengthened and bent the normal shock. From this time to about 2.7 seconds, that is when the normal shock and the two oblique shocks were about to move out of the nozzle exit plane, the back flow may have formed a triangular formation that sometimes was referred as the "teepees". In Fig. 7d, the normal shock has left the nozzle and developed a Mach disc at 3.17 seconds. This is consistent with the observation. The lip shock and the reflected shock were in the making. They were further developed at 3.50 seconds, as shown in Fig. 7e. The leading pressure wave has since arrived and past the rightmost grid domain.

The transient operation takes about 5 seconds to reach steady state. Fig. 7f shows the steady state pressure contours of the SSME firing at the sea level. This figure represents the same flowfield as that of Fig. 6. There is no flow separation observed at this point. The total CPU time was approximately 122 hours.

CONCLUSIONS

A time accurate, pressure based reactive CFD model FDNS has been developed to analyze a unified SSME liquid rocket engine flowfield. The flow domain included the combustion chamber, nozzle, exhaust plume and ambient. The code was validated through several systematic stages. For example, the FDNS predicted inviscid nozzle flowfields were first compared to those of the MOC, PARC, and RAMP solutions. The comparisons showed that the FDNS predictions were reasonably accurate for inviscid ideal gas and real gas cases. The viscous, real gas and specified wall temperature case have also shown excellent comparison in terms of Mach disc width and location to those of the hot fire test. Furthermore, the FDNS predicted SSME ISP values were in excellent agreement with those of the MOC and TDK predictions, and the Rocketdyne hot fire test data. A axisymmetric flow separation was also investigated through the transient thrust chamber and plume flowfield calculation. This first attempt demonstrated the capability of FDNS in studying the flow separation and shock evolution in the engine startup process.

REFERENCES

1. Wang T.S., Y.S. Chen, R.C. Farmer, and K. Tucker, "Numerical Investigation of the Transient SSME Fuel Preburner Combustor Flowfield," AIAA paper 90-0646, AIAA 28th Aerospace Sciences Meeting, Reno, Nevada, January, 1990.

2. Wang T.S., and Y.S. Chen, "A Unified Navier-Stokes Flowfield and Performance Analysis of Liquid Rocket Engines," AIAA paper 90-2494, AIAA/ASME/SAE/ASEE 26th Joint Propulsion Conference, Orlando, FL, July 1990.

3. Wang T.S., Y.S. Chen and R.C. Farmer, "Numerical Study of Ramjet Dump Combustor Flowfields with a Pressure Based CFD Method," AIAA paper 89-2798, AIAA/ASME/SAE/ASEE 25th Joint Propulsion Conference, Montery, CA, July 1989.

4. Chen, Y.S., and Kim, S.W., "Computation of Turbulent Flows Using an Extended k-ε Turbulence Closure Model," NASA CR-179204, Oct. 1987.

5. Launder, B.E. and D.B. Spalding, "The Numerical Computation of Turbulent Flows," Comp. Meth. Appl. Mech. Engr., 3, 269-289, 1974.

6. Chen, Y.S., "Viscous Flow Computations Using a Second-Order Upwind Differencing Scheme," AIAA Paper 88-0417, Jan. 1988.

7. Meintjes, K., and Morgan A.P., "Performance of Algorithms for Calculating the Equilibrium Composition of a Mixture of Gases," J. Comp. Physics, 60, pp. 219-234, 1985.

8. David, D., "Space Shuttle Engine Study," Vol. II, Interim Report, Contract 8-36176, Aerojet Tech. System Co., Sacramento, Ca., April, 1985.

9. Svehla, R.A., and B.J. McBride, "FORTRAN IV Computer Program for Calculation of Thermodynamic and Transport Properties of Complex Chemical Systems," NASA TN D-7056, Lewis Research Center, Cleveland, Ohio, 1973.

10. Cooper, G.K., "The PARC Code: Theory and Usage," AEDC-TR-87-24, Sverdrup Technology Inc., Oct. 1987.

11. Smith, S.D., "High Altitude Chemically Reacting Gas Particle Mixtures," Vol. I & II for RAMP2, LMSC-HREC TR D867400, Lockheed Huntsville Research Center, Oct. 1984.

12. SSME Engine 0005, 5000 seconds demonstration.

13. Neumeyer, R.K., SSME Performance and Decision Analysis, Rockwell International Corporation, Rocketdyne Division, Personal Communication, Nov. 1989.

CONTOUR LEVELS:

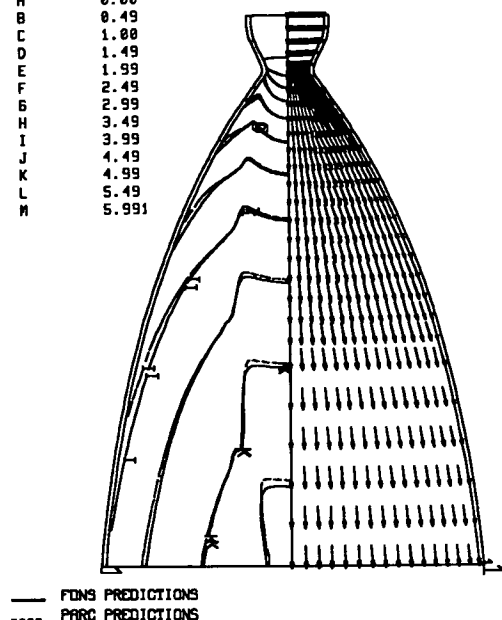| ID	VALUES
A	0.00
B	0.49
C	1.00
D	1.49
E	1.99
F	2.49
G	2.99
H	3.49
I	3.99
J	4.49
K	4.99
L	5.49
M	5.991

—— FDNS PREDICTIONS
---- PARC PREDICTIONS

Fig.1 Velocity vector and mach number contours
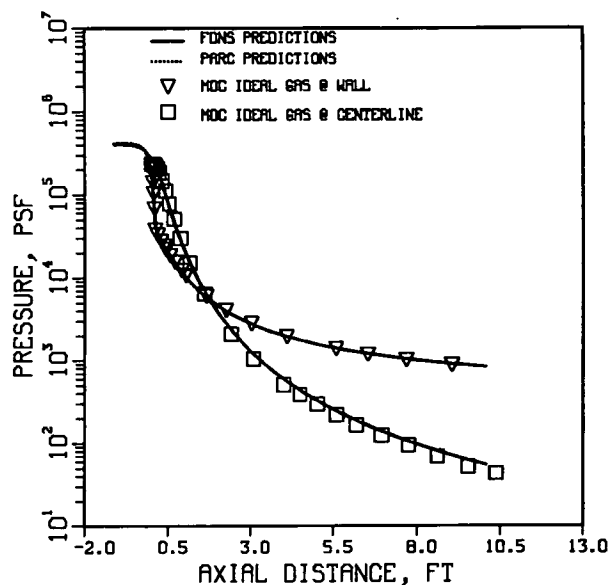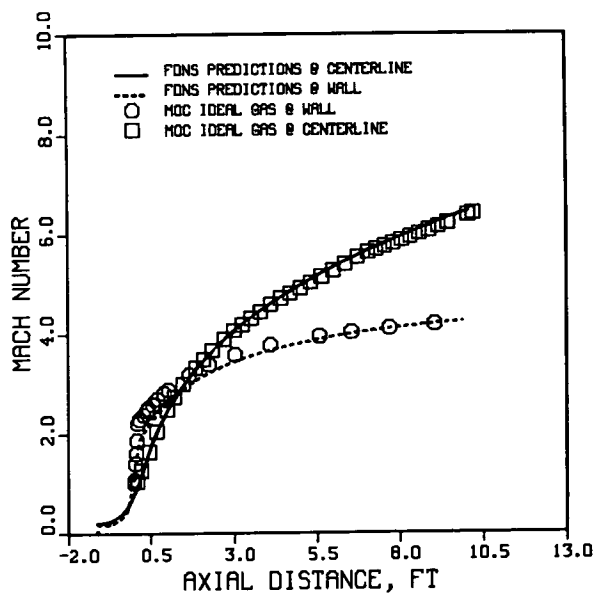for the inviscid, ideal gas (γ=1.1875) and
adiabatic wall SSME nozzle flowfield

Fig.2 Comparison of pressure distributions for
the inviscid, ideal gas (γ=1.1875) and adiabatic
wall SSME nozzle flowfield

Fig.3 Comparison of Mach numbers for the
inviscid, real gas and adiabatic wall SSME
nozzle flowfield
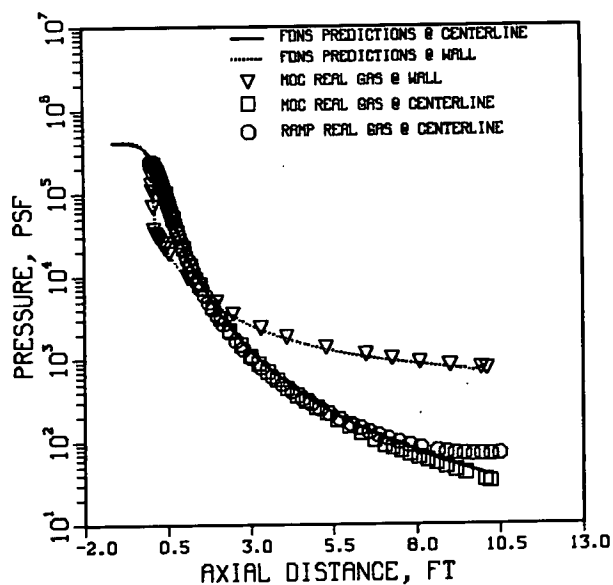
Fig.4 Comparison of pressure distributions for
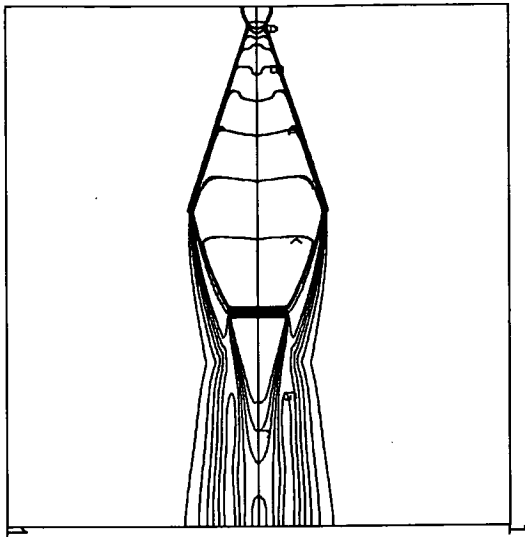the inviscid, real gas and adiabatic wall SSME
nozzle flowfield

141

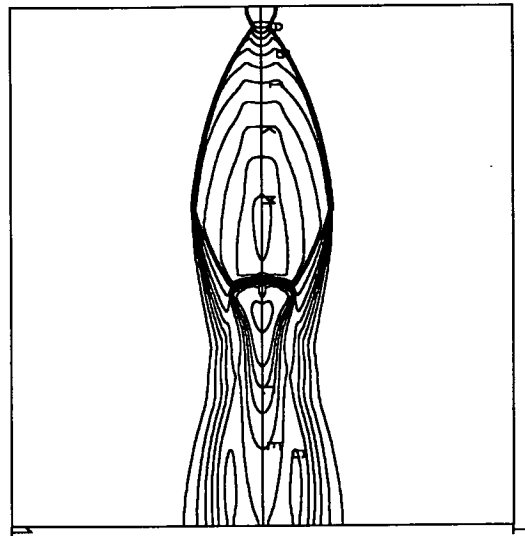Fig.5 The Mach number contours for a conical
nozzle flow

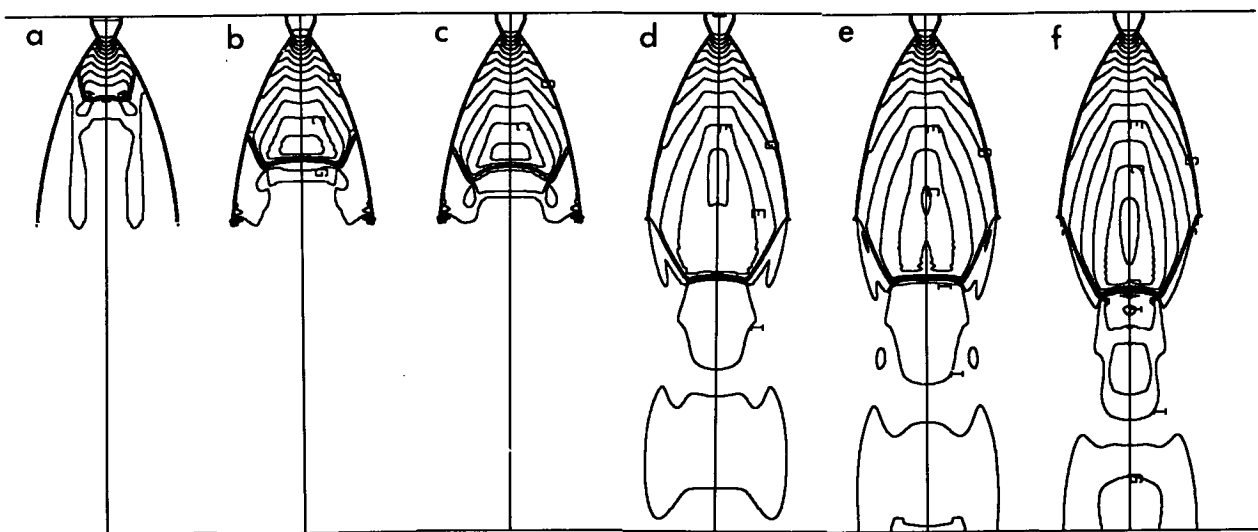Fig.6 The Mach number contours for the viscous,
real gas and specified wall temperature SSME
flowfield

Fig.7 Transient SSME pressure contour evolution